3D Microwave Imaging Using Huygens Principle: A Phantom-based Validation

B. Khalid[1], **B. Khalesi**[1, 2, 3], **N. Ghavami**[2, 3], **S. Dudley**[1], **M. Ghavami**[1], **and G. Tiberi**[1, 2, 3]

[1]School of Engineering, London South Bank University, London, UK
[2]Umbria Bioengineering Technologies, Perugia, Italy
[3]UBT UK Division, London, UK

Abstract— The main aim of this paper is to upgrade MammoWave acquisition and appropriately extend the Huygens Principle (HP) algorithm for allowing a 3D imaging reconstruction. The MammoWave device contains a cylindrical hub and two antennas, which are positioned at the same height and connected to a 2-port vector network analyser (Cobalt C1209, Copper Mountain, Indianapolis, IN). The two antennas can rotate azimuthally all around the object to be imaged. Measurements are performed recording the complex S_{21} in a multi-bistatic fashion. In this paper, we have performed a phantom-based investigation using a multi-quote scanning procedure via MammoWave operating at a 1–6.5 GHz frequency range. Specifically, a cylindrical phantom possessing a radius of 5.5 cm and height of 13 cm is constructed and a 3D structured volumetric flask with the spherical bottom (radius 1.75 cm) is used as inclusion. The materials and mixtures used in the preparation of the phantom have a contrast of 5 in dielectric properties. Next, measurements at planes along the z-axis are performed and multi-quote data are used in a modified version of the HP-based algorithm via superimposition theorem. The complex $6 \times 15 \times 80$ S_{21} is processed allowing 3D imaging reconstruction; our results clearly show the 3D visualisation of the detected inclusion at multiple planes. In more details, we verified that the dimension of the detected inclusion varies in the different planes of visualisation, accordingly to the spherical inclusion cross-section, with an average error in dimension qualification of $< 10\%$.

1. INTRODUCTION

Ultra-wideband (UWB) microwave imaging has been a new area of research in medical imaging due to the advantages related to its non-ionizing nature [1]. UWB microwave imaging is divided into two aspects concerning the ongoing research, which are UWB tomography and radar-based techniques. Among the radar-based technologies, the Huygens Principle (HP) based algorithm allows differentiation of healthy and malignant tissues in the frequency domain [2]. Lately, the HP-based microwave imaging algorithm has been applied for bone imaging, brain stroke imaging, and breast cancer detection [3–5]. The HP-based algorithm shows successful detection of the lesions in the 2D plane validated with the results [4, 5]. In addition to the mentioned methodologies, researchers are keen to investigate microwave imaging for 3D imaging as it would be very beneficial for locating the inclusion and detecting the dimensions of the inclusion [6]. Some of the research has been done and algorithms have been presented for brain stroke imaging and visualization in 3D [7].

Based on the HP microwave imaging algorithm, a novel, fast and accurate microwave imaging apparatus has been constructed by Umbria Bioengineering Technologies (UBT) Srl, Italy, named MammoWave, which is designed for breast cancer detection and is now under clinical trials producing one single 2D image in an azimuthal plane [8].

This paper proposes a new methodology, which includes the usage of the MammoWave device and its allowance to record the measurements in a multi-bistatic approach for 3D visualization. This paper demonstrates the capability of MammoWave to perform measurements at multiple planes along the z-axis for 3D visualization via superimposition theorem. The HP-based imaging algorithm has been modified from two dimensions to three dimensions and shows the potential for detecting the lesion in multiple planes and discovering the dimension of the inclusion with an error of $<$10%. The successful implication of the proposed methodology has been achieved and validated by the results obtained through performing the measurements on the fabricated phantom.

2. THEORY

For this study, a cylindrical phantom has been constructed along with the 3D structured volumetric flask as an inclusion. The dimensions of the cylindrical container, which is used as phantom and the 3D structured spherical inclusion, are shown in Figure 1. The purpose of using 3D structured inclusion is to implement the modified HP-based imaging algorithm via superimposition theory. The dimensions of the inclusion are the same from the tube cross-section but on going down vertically the diameter of the inclusion increases and become a sphere as shown in Figure 1(b). HP-based imaging algorithm differentiates the healthy and malignant tissues based on the difference in dielectric properties in the frequency domain. The mixture, which has been used to fabricate the phantom is TLe11.5c.045 oil provided from Zurich Med Tech Company (ZMT) with relative permittivity $\varepsilon r = 7$ [9]. The mixture of glycerol and water has been used as an inclusion possessing dielectric constant $\varepsilon r = 40$ at 2 GHz [10].

(a) (b)

Figure 1: (a) Fabricated Phantom, (b) 3D structured inclusion.

The fabricated inclusion is immersed 4.5 cm in the cylindrical phantom with the help of the lid having a hole, furthermore, the level of oil in the phantom and mixture in inclusion is aligned for better results.

MammoWave contains a cylindrical hub made of aluminium; the fabricated phantom having inclusion has been placed inside the cylindrical hub as shown in Figure 2. The device contains two antennas, which are positioned at the same height and connected to a 2-port vector network analyzer (Cobalt series, Copper Mountain, Indianapolis, IN) operating at the frequency range of 1–6.5 GHz [8].

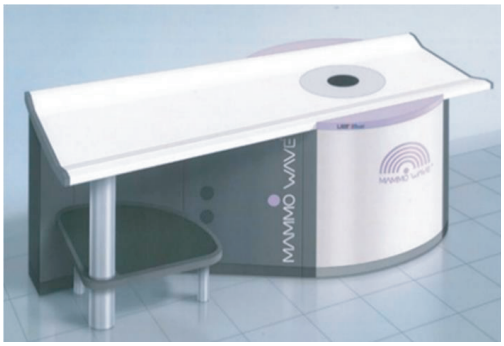

Figure 2: MammoWave Device by UBT Srl, Italy.

The measurements have been performed at multiple slices/cross-sections along the z-axis Z_h by computing the received signal S_{21} in a multi-bistatic way. The receiving points $N\mathrm{R}_x$ are equally spaced every 4.5°, leading to a total of $N\mathrm{R}_x = 80$ receiving points. Concerning the transmitting positions, all the experiments have been executed employing $N\mathrm{T}_x = 15$ transmitting positions,

displaced in 5 triplets centered at 0°, 72°, 144°, 216°, and 288°; in each triplet, the transmitting positions are displaced by 4.5°.

Let us consider the measuring setup in Figure 3 where the red dots represent the receiving points and the black dot depicting the transmitting points around the phantom [8]. The measurement process shown in Figure 3 is representing the measurement methodology for one plane and has been repeated for Z_h along the z-axis and S_{21} has been recorded similarly for each plane, whereas, $\mathrm{R}x_{n,h} \equiv (a_0, \emptyset_n, Z_h)$ and $\mathrm{T}x_{m,p,h}$ are the receiving and transmitting points at multiple planes Z_h respectively and a_0 is the radius of the cylindrical phantom.

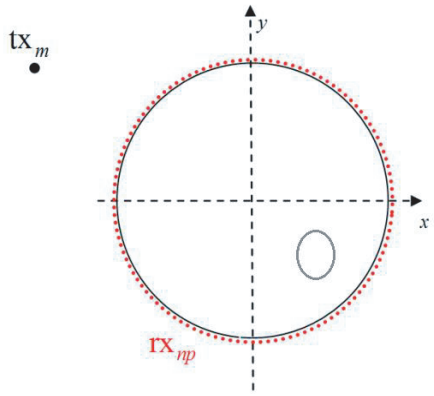

Figure 3: Pictorial view of the measurement process [8].

The received signal S_{21} measured at Z_h along the z-axis can be represented as ${S_{21}}_{n,h}^{m,p}(a_0, \emptyset_n, Z_h; tx_{m,p,h}; f)$ with $n = 1, 2, \ldots, 80$ indicating the receiving points; $m = 1, 2, \ldots, 5$ indicates the central transmitting positions, $p = 1, 2, 3$ indicates the positions inside transmitting sections, f is the frequency, and Z_h represents the multiple planes along the z-axis.

The data in the form of S_{21} for multiple planes have been processed through the HP-based imaging algorithm. The HP-based algorithm calculates the dielectric contrast between different mixtures under investigation, which in return helps to locate the inclusion in the frequency domain. The reconstructed '*rcstr*' electric field E for NPT observation points at multiple heights h_n (here we have performed measurements at 6 different heights), for frequency range (f) can be calculated as in Eq. (1).

$$E_{HP,3D}^{rcstr}(\rho, \emptyset, Z; tx_{m,p,h}; f) = \sum_{h=1}^{h_n} \sum_{n=1}^{NPT} {S_{21}}_{n,h}^{m,p}(a_0, \emptyset_n, Z_h; tx_{m,p,h}; f) G\left(k_1 \left|\overrightarrow{\rho_{n,h}} - \vec{\rho}\right|\right)$$

where $\overrightarrow{\rho_{n,h}} = (a_0, \emptyset_n, Z_h)$ are the observation points at multiple planes along the z-axis, $G(k_1|\vec{\rho}_{n,h} - \vec{\rho}|)$ is Green's function used to propagate the field and, k_1 indicates the wave number, which is set to be free space dielectric constant here. The string "HP" in $E_{HP,3D}^{rcstr}$ indicates that HP-based imaging procedure is employed in Equation (1). Hence using this information from the reconstructed field at multiple planes $h_n = 6$ over a number of frequencies (NF), a consistent image (I) can be obtained using Eq. (2).

$$I_{3D}(\rho, \emptyset, Z; tx_{m,p,h}) = \sum_{h=1}^{h_n} \sum_{i=1}^{NF} \left| E_{HP}^{rcstr}(\rho, \emptyset, Z; tx_{m,p,h}; f_i) \right|^2 \quad (1)$$

As images generated for multiple planes along the z-axis represent the cross-section measurements of the phantom with inclusion, the new modified HP-based imaging algorithm allows us to plot the images for each plane to analyze the dimension of the 3D structured inclusion at various planes via successful implication of the superimposition theorem.

3. RESULTS & DISCUSSIONS

This paper depicts the successful implication of the MammoWave in performing the measurements at multiple planes by changing the height of the transmitter and receiver antennas simultaneously.

As the aim of the study is to detect the inclusion [as shown in Figure 1(b)] at multiple planes along the z-axis and the dimension of the inclusion at each plane for 3D visualization.

For that purpose, we have performed several measurements at six different heights separated by 5 mm. As a reference, we assumed that quote n.6 represents the z-plane of the antennas crossing the middle of the spherical part of the inclusion, while other quotes are placed higher separated by 5 mm each. All the results have been generated using MATLAB after processing the S_{21} as given in Eq. (1) and Eq. (2). Figures 4(a), 4(b), and 4(c) show the detected inclusion at the various cross-sections of the 3D structured inclusion at multiple planes along the z-axis.

Since the measurements proceed towards the spherical part of the inclusion from the tube part, the detected inclusion is supposed to be bigger in dimensions than the previous one and ideally a spherical shape. Figure 4(c) presents the inclusion detected at the cross-section of the spherical part of the inclusion and demonstrates the increase in the size of detected inclusion showing the strong co-relation with the realistic inclusion. We have also performed image processing and adjusting for better 3D visualization and dimensional analysis for image quantification as shown in Figures 5(a), 5(b), and 5(c). The comparison between the detected inclusion and the realistic inclusion depicts the similarity regarding the dimensions of the inclusion. These multiple plane measurements and analysis of the inclusion at different cross-sections help us to visualize the inclusion in three dimensions along with the information of the dimensions of the inclusion.

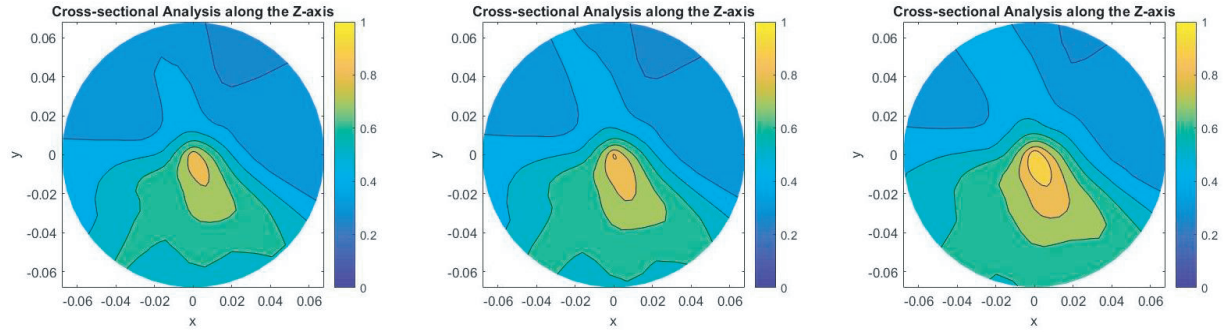

(a) (b) (c)

Figure 4: (a), (b), (c) show the detected inclusion from the cross-sectional analysis of the 3D structured inclusion at quote $n = 2, 4, 6$, respectively. Images are obtained following normalization to the global maximum value (x and y axes are given in meters).

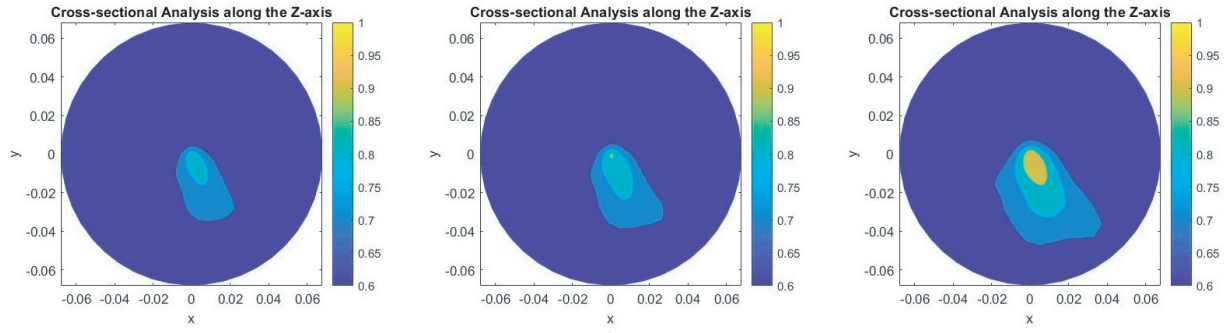

(a) (b) (c)

Figure 5: (a), (b), (c) show the detected inclusion from the cross-sectional analysis of the 3D structured inclusion at quote $n = 2, 4, 6$, respectively. Images are obtained following normalization to the global maximum value and forcing to zero the intensity values below 0.5 (x and y axes are given in meters).

We have quantified the obtained images by introducing dimensional analysis i.e., measuring the diameter of the detected inclusion and realistic inclusion to calculate the error between the different cross-sectional analyses. Image quantification shows that Figure 5(a) presents the cross-sectional analysis of the tube part of the inclusion having the diameter of 1 cm and Figure 5(b) presents the cross-sectional analysis of the start of the spherical part having the diameter of 2 cm approximately. Both results portray the resemblance in dimensions between the detected and realistic inclusion with

the error of less than 10% at each plane with different sizes of the inclusion. The detected inclusion in Figure 5(c) shows the spherical cross-sectional analysis with the 3.5 cm realistic diameter, but the error that appears in the dimensions of the detected inclusion is not more than 0.35 cm which makes the error percentage <10%.

4. CONCLUSION

This study focused on upgrading MammoWave acquisition and appropriately extending the HP algorithm for allowing a 3D imaging reconstruction. 3D imaging would be beneficial for allowing both 3D lesion localization and for extracting information about lesion dimensions. Specifically, we perform a phantom-based investigation using a multi-quote scanning procedure via MammoWave operating at 1–6.5 GHz frequency range. A cylindrical phantom possessing a radius of 5.5 cm and height of 13 cm is constructed and a 3D structured volumetric flask with the spherical bottom (radius 1.75 cm) is used as the inclusion. The liquids and mixtures used in the preparation of the phantom have a contrast of approximately 5 in dielectric constant. We verified that the dimension of the detected inclusion varies in the different planes of visualization, accordingly to the cross-section of the spherical inclusion, with an average error in dimension qualification less than 10%.

ACKNOWLEDGMENT

This project has received funding from the European Union's Horizon 2020 research and innovation program under grant agreements No: 830265, 872752, 101017098.

REFERENCES

1. Borja, B., J. A. Tirado-Méndez, and H. Jardon-Aguilar, "An overview of UWB antennas for microwave imaging systems for cancer detection purposes," *Progress In Electromagnetics Research B*, Vol. 80, 173–198, 2018.
2. Ghavami, N., G. Tiberi, D. J. Edwards, and A. Monorchio, "UWB microwave imaging of objects with canonical shape," *IEEE Transactions on Antennas and Propagation*, Vol. 60, No. 1, 231–239, 2012.
3. Tiberi, G., B. Khalesi, B. Sohani, S. Dudley, M. Ghavami, and N. Ghavami, "Phase-weighted UWB imaging through huygens principle," *2019 PhotonIcs & Electromagnetics Research Symposium — Spring (PIERS-Spring)*, 949–952, Rome, Italy, June 17–20, 2019.
4. Khalesi, B., B. Sohani, N. Ghavami, M. Ghavami, S. Dudley, and G. Tiberi, "Free-space operating microwave imaging device for bone lesion detection: A phantom investigation," *IEEE Antennas and Wireless Propagation Letters*, Vol. 19, No. 12, 2393–2397, 2020.
5. Sohani, B., J. Puttock, B. Khalesi, N. Ghavami, M. Ghavami, S. Dudley, and G. Tiberi, "Developing artefact removal algorithms to process data from a microwave imaging device for haemorrhagic stroke detection," *Sensors*, Vol. 20, No. 19, 5545. 2020.
6. Preece, A. W., I. Craddock, M. Shere, L. Jones, and H. L. Winton, "MARIA M4: Clinical evaluation of a prototype ultrawideband radar scanner for breast cancer detection," *Journal of Medical Imaging*, Vol. 3, No. 3, 033502. 2016.
7. Tobon Vasquez, J. A., R. Scapaticci, G. Turvani, G. Bellizzi, D. O. Rodriguez-Duarte, N. Joachimowicz, B. Duchêne, E. Tedeschi, M. R. Casu, L. Crocco, and F. Vipiana, "A prototype microwave system for 3D brain stroke imaging," *Sensors*, Vol. 20, No. 9, 2607, 2020.
8. Sani, L., N. Ghavami, A. Vispa, M. Paoli, G. Raspa, M. Ghavami, F. Sacchetti, E. Vannini, S. Ercolani, A. Saracini, and M. Duranti, "Novel microwave apparatus for breast lesions detection: Preliminary clinical results," *Biomedical Signal Processing and Control*, Vol. 52, 257–263, 2019.
9. Khalesi, B., B. Sohani, N. Ghavami, M. Ghavami, S. Dudley, and G. Tiberi, "A phantom investigation to quantify Huygens principle based microwave imaging for bone lesion detection," *Electronics*, Vol. 8, No. 12, 1505, 2019.
10. Meaney, P. M., C. J. Fox, S. D. Geimer, and K. D. Paulsen, "Electrical characterization of glycerin: Water mixtures: Implications for use as a coupling medium in microwave tomography," *IEEE Transactions on Microwave Theory and Techniques*, Vol. 65, No. 5, 1471–1478, 2017.